Received: 3 July 2024 | Revised: 21 September 2024 | Accepted: 27 September 2024

DOI: 10.1111/jace.20223

Journal of the American Ceramic Society

RESEARCH ARTICLE

Order evolution from a high-entropy matrix: Understanding and predicting paths to low-temperature equilibrium

Saeed S. I. Almishal[1] | **Leixin Miao**[1] | **Yueze Tan**[1] | **George N. Kotsonis**[1] | **Jacob T. Sivak**[2] | **Nasim Alem**[1] | **Long-Qing Chen**[1] | **Vincent H. Crespi**[1,3] | **Ismaila Dabo**[1] | **Christina M. Rost**[4] | **Susan B. Sinnott**[1,2] | **Jon-Paul Maria**[1]

[1]Department of Materials Science and Engineering, The Pennsylvania State University, University Park, Pennsylvania, USA

[2]Department of Chemistry, The Pennsylvania State University, University Park, Pennsylvania, USA

[3]Department of Physics, The Pennsylvania State University, University Park, Pennsylvania, USA

[4]Department of Materials Science and Engineering, Virginia Polytechnic Institute and State University, Blacksburg, Virginia, USA

Correspondence
Saeed S. I. Almishal, Department of Materials Science and Engineering, The Pennsylvania State University, University Park, PA, USA.
Email: saeedsialmishal@gmail.com

Equal author contribution. Saeed S. I. Almishal and Leixin Miao

Funding information
National Science Foundation, Grant/Award Number: 2011839

Abstract

Interest in high-entropy inorganic compounds originates from their ability to stabilize cations and anions in local environments that rarely occur at standard temperature and pressure. This leads to new crystalline phases in many-cation formulations with structures and properties that depart from conventional trends. The highest-entropy homogeneous and random solid solution is a parent structure from which a continuum of lower-entropy offspring can originate by adopting chemical and/or structural order. This report demonstrates how synthesis conditions, thermal history, and elastic and chemical boundary conditions conspire to regulate this process in $Mg_{0.2}Co_{0.2}Ni_{0.2}Cu_{0.2}Zn_{0.2}O$, during which coherent CuO nanotweeds and spinel nanocuboids evolve. We do so by combining structured synthesis routes, atomic-resolution microscopy and spectroscopy, density functional theory, and a phase field modeling framework that accurately predicts the emergent structure and local chemistry. This establishes a framework to appreciate, understand, and predict the macrostate spectrum available to a high-entropy system that is critical to rationalizing property engineering opportunities.

KEYWORDS
epitaxy, high-entropy oxides, nanostructures, phase-field modeling, TEM

1 | INTRODUCTION

Solid solutions comprise a formulation space from which cornerstone material technologies spanning mechanical, optical, electronic, electromechanical, and memory applications routinely emerge.[1–3] Examples of note include high-strength-to-weight ratio alloys based on Al-Si,[4] high-speed microcircuits on a Si-Ge platform,[5] solid-state lasers built from $Al_{1-x}Ga_xN$ heterostructures,[6] extreme-strain actuators from $(PbMg_{1/3}Nb_{2/3}O_3)_{1-x}(PbTiO_3)_x$ single crystals,[7] and recently, Si-compatible ferroelectric thin films of $Al_{1-x}Sc_xN$[8] and $Al_{1-x}B_xN$.[9] The value afforded by these systems is the overarching ability to continuously tune composition between end members and subsequently

vary structures and properties either smoothly between the two compositional bounds (as in GaAs-AlAs),[10] or through often-surprising maxima (as in $PbTiO_3$-$PbZrO_3$).[11] Both categories yield rich science, property, and performance rewards.

Historically, the solid solution selection process uses isostructural end members, or end members whose elemental constituents share reasonably similar electronegativities, radii, and/or polyhedral coordination to a common cation or anion. Classical criteria such as Goldschmidt's tolerance factor,[12] Hume-Rothery rules,[13] and Pauling's rules[14] provide excellent frameworks that guide selection. These frameworks favor structures with a large negative formation enthalpy, thus the compositional solubility spectrum they predict will directly reflect the dispersity of elemental periodic properties.[15,16] That is to say, only a finite number of enthalpy-driven combinations exist that afford extensive solubility windows because elemental properties vary rapidly along most directions of the periodic table.[3,16]

Initiated by interest in amorphous metals, researchers in the 1990s began exploring formulation spaces involving five or more components with comparable mole fractions in a deliberate effort to maximize configurational disorder through chemistry.[1,3] Many diverse metal atoms on a single sublattice will boost configurational entropy and, with increasing temperature, will thermodynamically stabilize the single-phase solid solution. The pioneering works of Cantor[17] and Yeh [18] exemplify this approach. The same possibility was demonstrated by Rost et al. in 2015, with direct proof of entropic stabilization in complex oxides.[19] Comparable reports for carbides, borides, sulfides, and nitrides followed soon thereafter.[3] There are now many reports for high-entropy compositions that solubilize metal cations in unusual local coordinations and structural distortions that are associated with interesting property responses; examples include an energy landscape promoting ion migration or ion valence distributions that tune the electronic band gap.[3,20,21]

These observations lead to an alternative perspective for high configurational entropy materials, one considering them as solid solutions in a composition landscape with boundaries well beyond the Hume-Rothery or Pauling limits. With this high configurational entropy by formulation, the equilibrium temperature between enthalpic or entropic victory is within or close to practical synthesis limits, that is, before problematic melting, volatilization, or metal reduction. Consequently, the highest-entropy "parent" solid solution—that features a homogeneous and random elemental distribution—can be preserved at room temperature by quenching into a metastable state. This disordered parent is linked thermodynamically to a continuum of offspring sub-structures that are accessible through engineered thermal histories. Each offspring represents the outcome of an entropy-enthalpy exchange to an increasingly ordered state. This perspective is fundamentally the same one used to understand phase evolution in metal alloys,[22] however, the higher diversity of metal cations in a high-entropy oxide (HEO) offers more degrees of freedom during the return to thermal equilibrium. Stated alternatively, such materials have more ways to spend their entropy.

We focus on the original high-entropy and entropy-stabilized oxide, $Mg_{0.2}Co_{0.2}Ni_{0.2}Cu_{0.2}Zn_{0.2}O$ that adopts an equilibrium rock salt solid solution structure above ~875°C with all cations in octahedral coordination and no evidence of intermediate or long-range elemental clustering.[19,23] For all HEOs that are entropy stabilized above room temperature, such as $Mg_{0.2}Co_{0.2}Ni_{0.2}Cu_{0.2}Zn_{0.2}O$, some degree of quenching is needed to lock a metastable configurational microstate at room temperature, representative of the high-temperature solid solution macrostate.[3,24,25] In our experience, normal furnace cooling at ~10°C/min is sufficiently rapid, and years of dwell time at room temperature does not produce measurable structural changes. However, phase decomposition studies on bulk samples demonstrate that intermediate temperatures (roughly 300–850°C) result in CuO precipitation within several hours.[26,27] This could be due to Cu-Cu pair interactions that reduce the total energy as they create new and unique lower-configurational-entropy macrostates.[28–31] Additionally, a spinel phase, attributed to Co_3O_4 , begins to form in bulk samples when annealed at intermediate temperatures in air.[31]

We explore the continuum of new states that emerge when a metastable high-entropy solid solution approaches equilibrium upon "fluid" exchange between entropic disorder and enthalpic return. For a system to approach equilibrium, the reduction in total free energy density requires that the enthalpic return must be greater than the entropic spending. In other words, at a temperature T below the entropic-stabilization temperature, the reduction in enthalpy ΔH resulting from the formation of secondary ordered phases must be sufficient to outweigh the concurrent reduction in $T\Delta S$, where ΔS is the change in entropy. This is necessary to ensure a net reduction in the system's Gibbs free energy ($\Delta G = \Delta H - T\Delta S < 0$). In Figure 1, we use a tangible analogy by presenting the system's available entropy and thermal energy as "TS currency bags", symbolizing the entropy cost necessary to achieve a greater enthalpic return. Essentially, a portion of the initial entropy in the single-phase high-entropy state must be spent to purchase and attain a higher degree of order and enhanced overall system stability at our synthesis conditions. The right end member

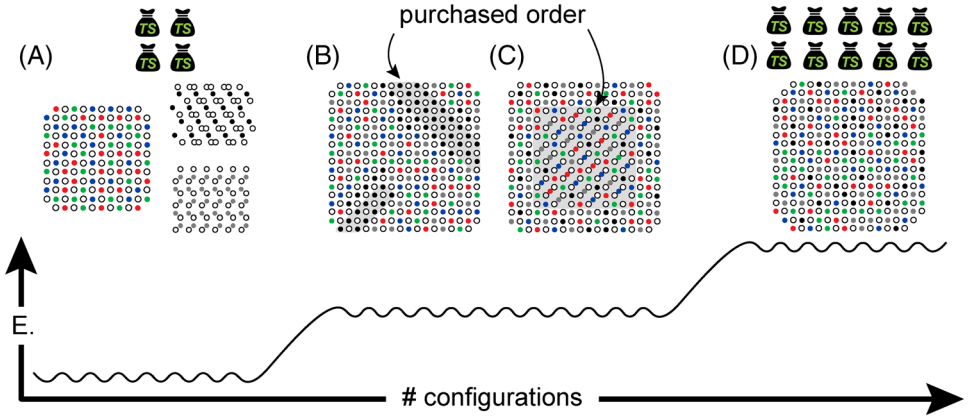

FIGURE 1 Qualitative depiction of possible atomic configurations in a rock salt high-entropy oxide (HEO) different in total energy, E, plotted along one hypothetical pathway through configuration space. (A) represents a low-configurational-entropy state, including a three-component rock salt solid solution and two other phases with different crystal structures each with a single cation; (B) a middle region with intermediate entropy featuring chemical segregation of a particular species concentrated nanoregions; (C) a second intermediate region featuring nanoregions where some of the octahedral cations shift to tetrahedral interstitial sites without chemical ordering; and (D) the most entropy-rich state where five cations randomly occupy a single sublattice with no regular chemical ordering. TS bags serve as an analogy for the concept of spending entropy discussed in the main text.

in Figure 1 represents the most entropy-rich state where five cations randomly occupy a single sublattice with no regular chemical ordering (Figure 1D), while the left end member represents a much lower-entropy state featuring chemical clustering and multiple phases (Figure 1A). The region of present interest is the center, where more subtle hypothetical entropy spending occurs to chemically segregate a particular species (Figure 1B) or to locally induce point defects involving specific cation species (Figure 1C). Importantly, for the latter two examples, the anion sublattice is unchanged and the boundaries to new, partially ordered structures are coherent and defect-free.

Interest in these still-coherent macrostates is predicated on an expectation that local distortions associated with phase instability will lead to new property possibilities. For example, magnetic and electron-correlated properties are sensitive to highly localized exchange interactions that may be enhanced by entropy-reducing reconfigurations.[32–34] A particularly compelling case is the nucleation of spinel phases within a rock salt matrix, which could result in unique magnetic phases.[32,35–38] Another notable example is the influence of short-range order on electrochemical performance—it can either limit battery recharge cycles[39] or enhance reversible oxygen uptake and rejection cycles for high-efficiency water splitting.[40] Inspired by these and similar examples, we develop a predictive understanding for evolving order in high-entropy materials from a quenched metastable state and report how offspring macrostates, featuring partially-ordered coherent nanostructures, emerge at the nanometer scale.

2 | THE EXPERIMENT: EXPLORING KINETIC PATHWAYS TO ORDER DURING SYNTHESIS

In principle, a specimen's atomic configuration and physical properties depend on synthesis conditions, which vary widely in kinetic terms.[3] Physical vapor deposition techniques such as sputtering and pulsed-laser deposition (PLD) produce gas phase particle ensembles with eV-level kinetic energies (10^4–10^5 K effective temperature) that equilibrate to $k_B T_{substrate}$ conditions just nanoseconds after substrate landing, which can secure a metastable but persistent high-energy structure.[3,31,41,42] PLD is particularly well suited to explore these macrostate possibilities by establishing pulse rate, laser energy density, substrate temperature, and deposition pressure combinations that, for example, change average growth rate dramatically, while leaving adatom landing energy unchanged. In general pulse rate controls the time interval between adlayer accumulation where comparatively rapid surface diffusion mechanisms remain active, substrate temperature governs thermal vibrational entropy, film thickness regulates epitaxial strain accumulation, and pressure can regulate kinetic energy thermalization. Using such capabilities, we demonstrate nanostructure engineering within $Mg_{0.2}Co_{0.2}Ni_{0.2}Cu_{0.2}Zn_{0.2}O$ arising from the growing film's desire to approach equilibrium under these different mobility and driving force conditions.

We demonstrate nanostructure evolution through the entropy-enthalpy exchange in epitaxial $Mg_{0.2}Co_{0.2}Ni_{0.2}Cu_{0.2}Zn_{0.2}O$ thin films grown with PLD on warm substrates (~400°C). The laser repetition rate,

which controls the average accumulation rate of material, varied between 1 and 5 Hz, and the deposition duration, which is quantified by the total number of laser pulses, varied between 1200 and 6000 pulses. Using these conditions, the following film categories are created: **i**. thin and fast; **ii**. thin and slow; **iii**. thick and fast; and **iv**. thick and slow. Films from the four categories are denoted as 1200–5, 1200–1, 6000–5, and 6000-1 Hz, respectively. In this series, thin versus thick delineates materials with different quantities of epitaxial and thermal expansion mismatch-induced stored elastic strain energy, while slow versus fast delineates materials with more or less time available for "annealing/relaxation" between flux pulse events.

X-ray diffraction (XRD) scans provide the initial structural information for films prepared using these conditions. Figure 2A shows the 1200-5, 1200-1, and 6000–1 Hz films exhibit single-phase rock salt structures with pronounced thickness fringes suggesting high crystalline fidelity. The 6000–5 Hz film exhibits an additional peak suggesting an additional phase. Reciprocal space maps of the (204) reflections in Figure 2B–E indicate that all films are epitaxially strained with the same in-plane lattice parameter as the MgO substrate (4.21 Å). Calculations from out-of-plane scans reveal out-of-plane lattice constant values of 4.27 Å (1200–5 Hz), 4.28 Å (1200–1 Hz), 4.27 Å and 4.25 Å (6000–5 Hz), and 4.27 Å (6000–1 Hz). The laboratory XRD analysis indicates noteworthy structural changes for the different deposition conditions, despite the same overall deposition flux and the same substrate temperature.

Scanning transmission electron microscopy is used to explore structural features and local chemistry at the atomic scale. This technique is critical because, especially at the onset of order, longer-range probes like diffraction will have great difficulty resolving structural changes. Representative samples from the four categories were examined. The 1200–5 Hz film selected area electron diffraction (SAED) pattern shows sharp diffraction spots indicating a pristine rock salt crystal (Figure 2F). The annular dark-field scanning transmission electron microscopy (ADF-STEM) micrograph appears featureless, and the higher magnification inset shows an abrupt epitaxial interface and a clearly defined rock salt lattice (Figure 2I). The 1200–1 Hz film low-angle annular dark-field STEM (LAADF-STEM) micrograph shows high-contrast striations indicative of local lattice strain aligned to the {101} planes in real space (Figure 2J) and the SAED pattern (Figure 2G) shows streaking in all < 101 > reciprocal lattice directions which is a "tweed" nanostructure signature. This tweed nanostructure is often reported in cubic alloy systems due to the formation of tetragonally distorted platelets.[43,44] The 6000–5 Hz film LAADF-STEM mode (Figure 2K) reveals starkly different features: a high density of nanoscopic cuboids that distribute randomly throughout the rock salt matrix (Note S1). The 6000–5 Hz film SAED pattern (Figure 2H) exhibits extra spots forbidden in rock salt crystals, appearing at $\vec{g} = \{101\}$ (Figure 2H inset). The alignment of these spots relative to the matrix indicates an epitaxial orientational arrangement in three dimensions.

2.1 | Local symmetry and chemical analysis: (a) CuO-rich nano tweeds

Figure 3A presents a magnified ADF-STEM image of the 1200–1 Hz film, showing the atomically resolved morphology of the nanoscale tweed microstructure. EDX mapping (Figure 3C) reveals an enrichment of Cu ions and a deficiency of Mg, Co, Ni, and Zn ions within the platelets. Unsupervised machine learning-based local symmetry analysis (Note S2) was employed to categorize the local Fourier-transform (FT) patterns collected from Figure 3A into three classes: T1, a CuO-rich zone with an orientation pointing down and right; T2, a CuO-rich zone with an orthogonal orientation to T1; and RS, the rock salt matrix with no nanostructuring (Figure 3B). Further analysis of T1 and T2 reveals lattice rotation and tetragonal distortions consistent with observations of Jahn-Teller distorted CuO_6 octahedra in $Mg_{0.2}Co_{0.2}Ni_{0.2}Cu_{0.2}Zn_{0.2}O$[23,45,46] (described in detail in Note S2).

2.2 | Local symmetry and chemical analysis: (b) spinel-like nanocuboids

Figure 4A shows a higher-magnification atomically-resolved ADF-STEM image for the 6000–5 Hz film highlighting one of the nano-cube regions. The magnified inset reveals additional periodic cation columns inside the cuboid. These locations correspond to the tetrahedral interstitials of the oxygen sublattice in rock salt (Fm $\bar{3}$ m symmetry) are unoccupied. Populating these sites periodically will produce the spinel structure (Fd $\bar{3}$ m symmetry). There is precedent for such spinel-type clusters in rock salt matrices as in defect clusters in wüstite $Fe_{1-x}O$[47] and lithium manganese oxide.[48] Our recent work has additionally demonstrated that when a sintered single-phase bulk sample is annealed at or below 700°C, a secondary spinel phase begins to form.[31] To further investigate the spinel formation in the thin films, local symmetry analysis was applied to categorize the local FT patterns collected from Figure 4A into two classes: RS, a rock salt matrix with no apparent nanostructuring; and SP, a spinel-structured region (Figure 4B) (described in detail in Note S2).

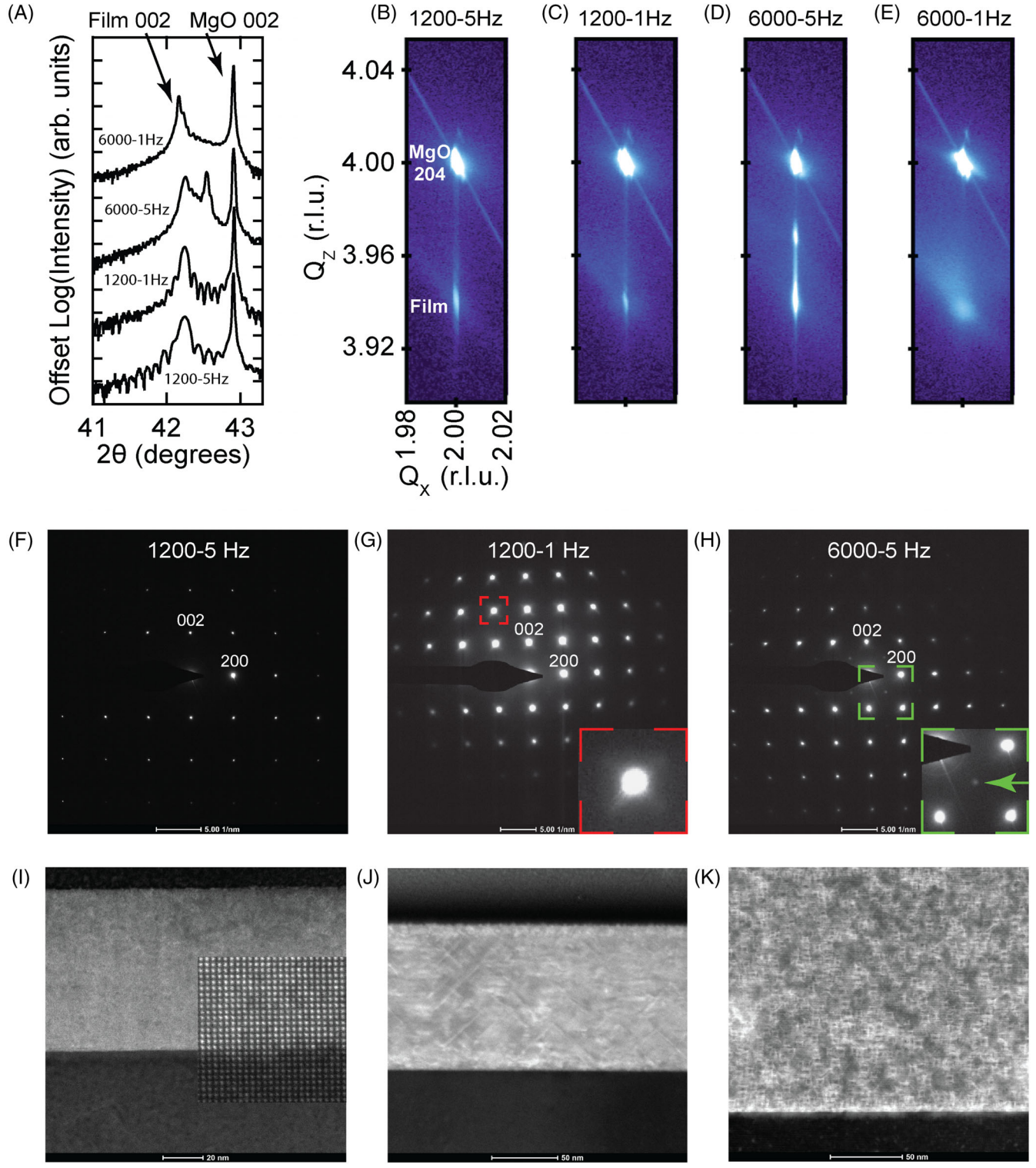

FIGURE 2 Out-of-plane X-ray diffraction (XRD) patterns (A) and reciprocal space maps (B–E) of the four film categories. 1200–5, 1200–1, and 5000–5 Hz exhibit single-phase rock salt structures with pronounced thickness fringes and high crystalline fidelity. 6000–5 Hz exhibits an additional peak. Reciprocal space maps of the (204) reflections indicate that 1200–5, 1200–1, and 6000–5 Hz are epitaxially strained with the same in-plane lattice parameter as the MgO substrate. Transmission electron microscopy (TEM) analysis showing (F–H) selected area electron diffraction (SAED) patterns 1200–5, 1200–1, and 6000–5 Hz with insets highlighting the streaking and additional diffraction spots (acquired from the [010] zone axis); and (I–K) annular dark-field scanning transmission electron microscopy (ADF-STEM) images for the same samples showing a uniform structure in 1200–5 Hz and nanostructure development in 1200–1 Hz (nano tweed morphology) and 6000–5 Hz (nano-cuboid morphology). (J, K) were collected in low-angle annular dark-field STEM (LAADF-STEM) mode to highlight strain contrast.

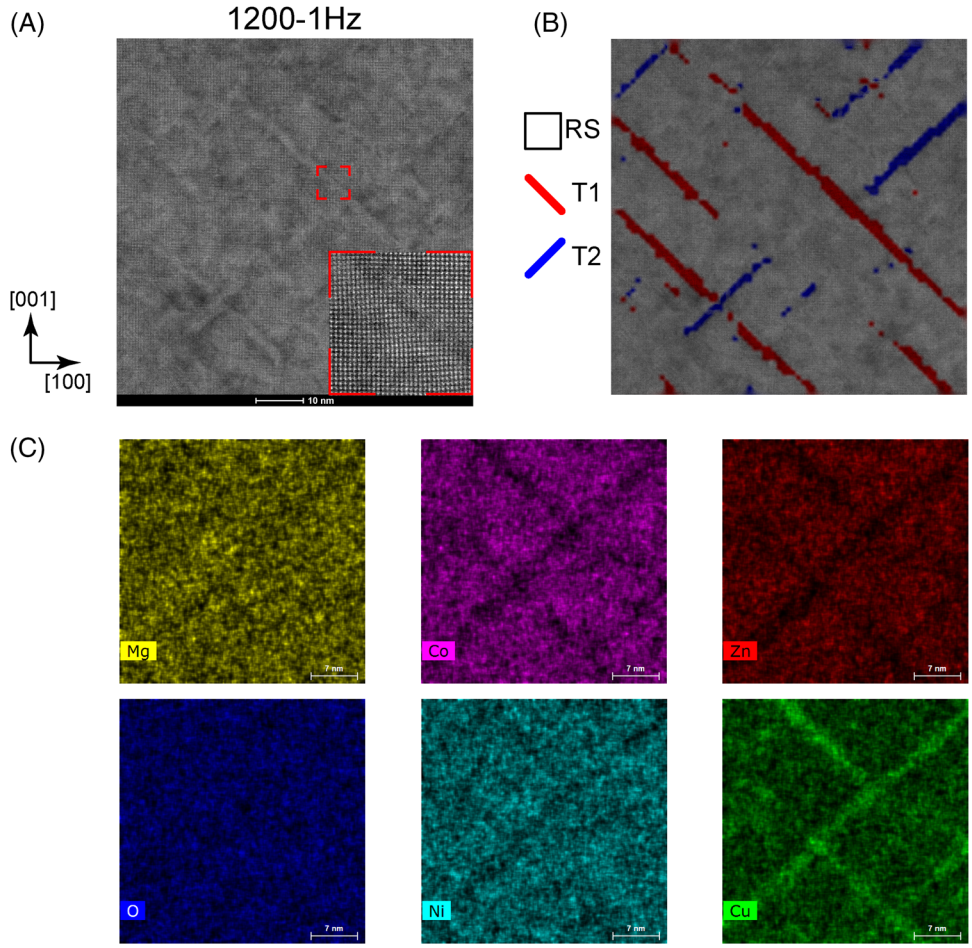

FIGURE 3 Local structural and chemical analysis of $Mg_{0.2}Co_{0.2}Ni_{0.2}Cu_{0.2}Zn_{0.2}O$ grown at a 1 Hz pulse rate using 1200 total pulses: (A) annular dark-field scanning transmission electron microscopy (ADF-STEM) image and magnified inset of a tweed region; (B) results of image segregation based on local symmetry analysis with overlayed colors representing the rock salt matrix (RS, colorless) and tweed platelets oriented in two directions (T1 in red and T2 in blue); and (C) representative energy-dispersive X-ray (EDX) map showing that the tweeds are primarily rich in Cu.

Additional analysis on the coherent spinel nano-cuboids reveals a 2% lattice parameter reduction in both in- and out-of-plane directions not detected by XRD analysis. However, XRD shows two strong peaks in 2θ indicating an epitaxial material with the expected pristine rock salt out-of-plane lattice constant and a second out-of-plane lattice constant that is 0.5% smaller. We attribute the second XRD peak to the heavily nanostructured rock salt matrix near the substrate interface (Note S1).

Ideal spinel structures exhibit A_3O_4 stoichiometry, necessitating some fraction of 3+ cations. Thus, we employed spatially resolved monochromated STEM-EELS to probe the energy loss near edge structure (ELNES) of the transition metal elements. Class-averaged electron energy loss spectra (EELS) for the oxygen K edge ELNES and Co L edge ELNES spectra are plotted in Figure 4C,D. An additional peak in the oxygen K spectra appears at approximately 531 eV in spinel-containing regions in Figure 4C, indicating additional empty states in the transition metal 3d orbitals compared to RS regions. Ni and Cu ELNES spectra show no significant change (Note S3). However, the Co ELNES of SP regions closely resembles the reference ELNES spectra of spinel Co_3O_4, while the RS regions agree well with the rock salt CoO ELNES reference.[37,38] These results suggest that Co^{3+} ions are responsible for accommodating the local symmetry change and producing the additional empty 3d states found in the oxygen K spectra.

2.3 | Local symmetry and chemical analysis: (c) CuO nanotweeds and spinel-like nanocuboids

If a slow growth rate and a significant film thickness are indeed critical factors for the formation of CuO nanotweeds and spinel epitaxial nano-cuboids, respectively,

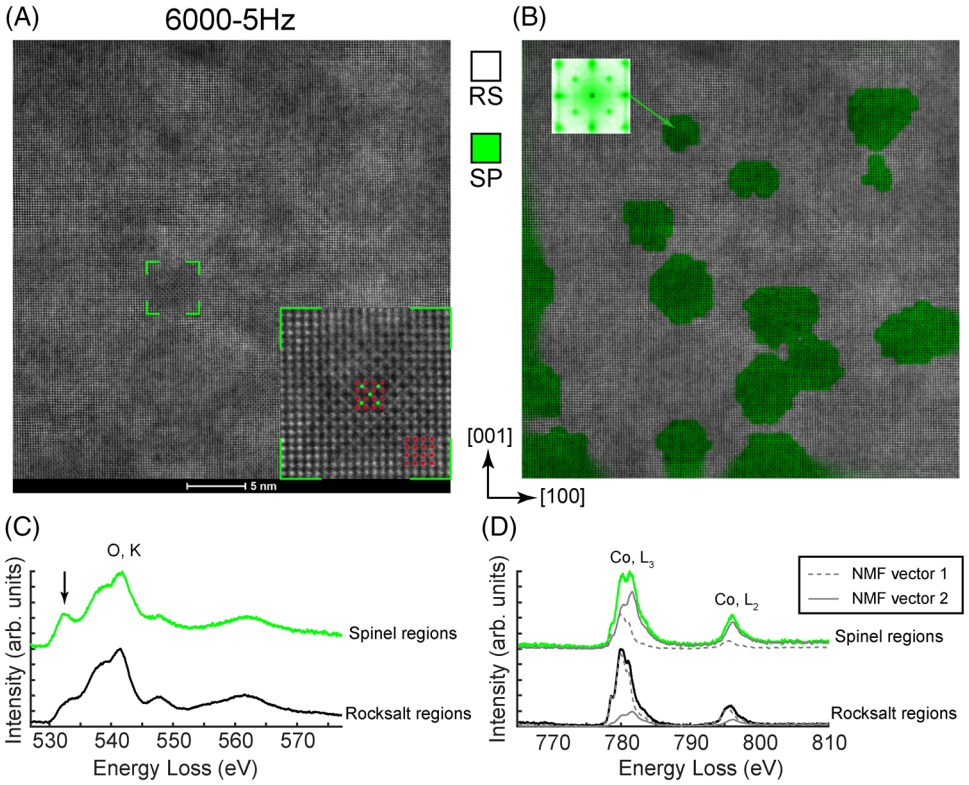

FIGURE 4 Local structural and chemical analysis of $Mg_{0.2}Co_{0.2}Ni_{0.2}Cu_{0.2}Zn_{0.2}O$ grown at a 5 Hz pulse rate using 6000 total pulses: (A) annular dark-field scanning transmission electron microscopy (ADF-STEM) image and magnified inset of a spinel nano-cuboid region; (B) Results of image segregation based on local symmetry analysis with overlayed colors representing rock salt matrix (RS, colorless) and spinel nano-cuboids (SP, green) with SP class averaged Fourier transform shown in the inset; (C) class-averaged O K edge energy loss near edge structure (ELNES); and (D) class-averaged Co L edge ELNES from the SP regions (green) and RS regions (black). Class-averaged ELNES spectra were decomposed as the linear combination of two nonnegative matrix factorization (NMF) loading vectors, plotted in (D) with dashed and solid gray lines. These NMF vectors bear a striking resemblance to CoO and Co_3O_4 reference spectra (Note S3).

rather than merely probabilistic occurrences, a thick and slowly grown film should possess both features. Figure 5 depicts the TEM analysis of this 6000–1 Hz sample. The SAED pattern (Figure 5A) taken from a location near the substrate interface shows streaking along $< 101 >$ in reciprocal space and extra reflections at $\vec{g} = \{101\}$ validating our hypothesis. The $\vec{g}_{002}$ and $\vec{g}_{10\bar{1}}$ reflections were isolated to collect dark field TEM (DF-TEM) micrographs that reveal the spatial distribution of tweed platelets (Figure 5B) and spinel nano-cuboids (Figure 5C) respectively. Figure 5D shows the results of the TEM image segregation with both nanostructures (more analysis in Notes S1, S2, and S4).

3 | MULTI-PHYSICS MODELING FOR EVOLVING ORDER

While nanostructure formation can be rationalized by the entropy spending analogy as discussed in Figure 1, their evolution is more complex. This evolution is accompanied by the formation of interfaces, inhomogeneous stress/strain fields, and inhomogeneous chemical compositions—the nanostructures evolve to minimize the total free energy of the system comprising interfacial energy, strain energy, and chemical energy. To predict and analyze the morphological evolution, we developed a phase-field model for the HEOs films, independent of the PLD plasma plume dynamics. This model incorporates the key thermodynamic contributions and density functional theory (DFT)-calculated lattice parameters and elastic constants, as detailed in Notes S6 and S7. Temporal evolution and growth of the CuO-nano tweeds and spinel nano-cuboids from phase-field simulations are depicted in Figure 6. The predicted morphological evolution agrees with experimental observations by STEM in Figures 3 and 4, in both geometry and dimension. Strain mapping and total energy analysis for both nanostructure types are presented and discussed in detail in Note S5. Overall, phase-field simulations support the postulate that the reductions in chemical and elastic strain energy are nanostructure influencers that drive exsolution in $Mg_{0.2}Co_{0.2}Ni_{0.2}Cu_{0.2}Zn_{0.2}O$.

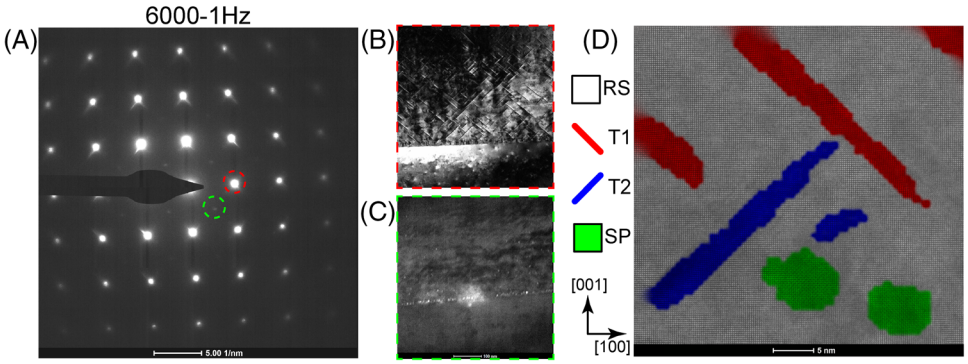

FIGURE 5 Structural and chemical analysis of $Mg_{0.2}Co_{0.2}Ni_{0.2}Cu_{0.2}Zn_{0.2}O$ grown at a 1 Hz pulse rate using 6000 total pulses: (A) Selected area electron diffraction (SAED) pattern acquired at the interface of the film; (B) and (C) dark field TEM (DF-TEM) images showing the tweed structures and spinel nano-cuboids respectively, acquired using and reflections [red and green circles in (A)]; (D) results of image segregation based on local symmetry analysis with overlayed colors representing rock salt matrix (RS, colorless), tweed structures oriented in two directions (T1 in red and T2 in blue), and spinel nano-cuboids (SP, green).

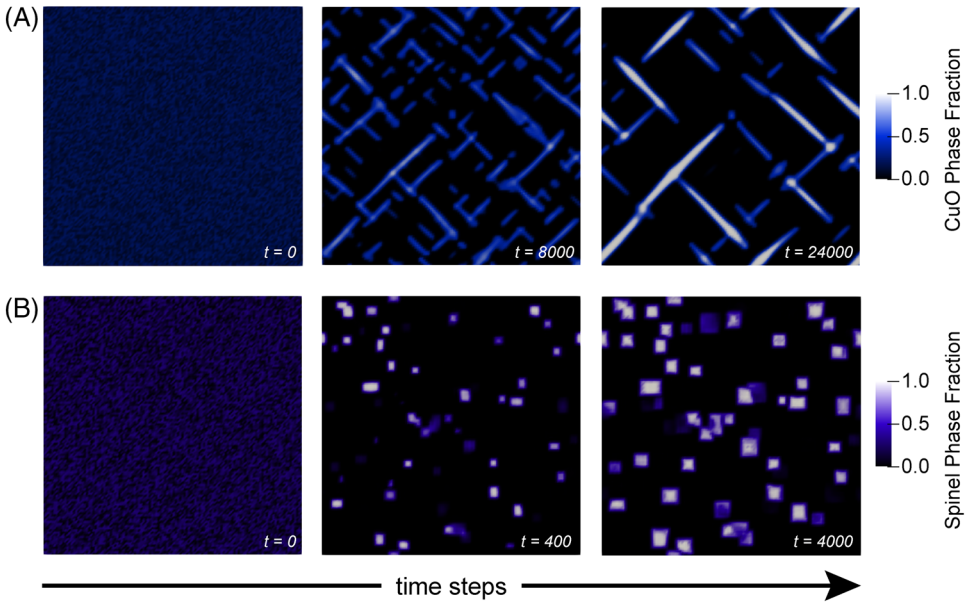

FIGURE 6 Phase-field simulations of the morphologies of (A) CuO-rich tweed patterns, and (B) spinel nanocuboids in $Mg_{0.2}Co_{0.2}Ni_{0.2}Cu_{0.2}Zn_{0.2}O$. Cross-sectional images from 3D simulations are captured at y = 50 nm. Temporal evolutions are carried out with discretized time steps of fixed lengths. A number of time steps for the displayed frames are labeled with inset text.

The CuO segregation and redistribution are driven by the chemical energy reduction overcoming the increase in the interfacial energy and the strain energy associated with maintaining a coherent nanostructure. We only observe CuO nanotweeds in thin films where inter-pulse anneal is 5 times longer, suggesting that its kinetics are limited by the slow diffusion of CuO in the rock salt matrix. The tweed shape (Figure 6A) is a consequence of the anisotropic stress-free transformation strain (SFTS) arising from the tetragonal Jahn-Teller distortion of the CuO relative to the cubic rock salt matrix. The simulated nanotweed structure tilt is 43° relative to rock salt (001), in quantitative agreement with our TEM analysis (45°) and microelasticity theory calculations (44°).[22]

The spinel-nanocuboids are only observed in coherent thick films where the elastic strain energy per unit area is ~5 times larger than in the thinner films. The large compressive elastic strain energy in the thicker films favors Co^{3+} due to its ~18% smaller ionic radii compared to Co^{2+}.[37] A complementary explanation is that Co favors a 3+ oxidation state at our growth conditions (400°C, but well below the solid solution stability threshold of

875°C and a high oxygen chemical potential).[31,37] Thus, the increased strain within thick films mediates its transition from quenched and trapped Co^{2+} to enthalpy-favored Co^{3+} at our growth temperature and pressure. We speculate that the following defect chemical process accompanies this conversion to conserve charge, mass, and lattice site ratios:

$$Co^{x}_{Co^{2+}} \Rightarrow Co^{3+\cdots}_{i_{tetrahedral}} + V''_{M} + e'$$

This site occupancy and oxidation state change of Co into the newly unlocked tetrahedral sites produces the chemically-driven and enthalpy-favored spinel phase. Collectively, the inclusion of Co^{3+}-containing spinel nanostructure within the rock salt matrix affords an overall reduction of strain energy for the thicker films (discussed in detail in Note S5). The cubic-to-cubic transformation of spinel nano-cuboids induces isotropic SFTS, resulting in overall smaller elastic anisotropy compared to the anisotropic SFTS of CuO-tweeds (cubic-to-tetragonal). The elastic anisotropy of the spinel phase, however, is due to the anisotropic elastic stiffness, which is defined for a cubic crystal as[22]:

$$\zeta = \frac{c_{11} - c_{12} - 2c_{44}}{c_{44}}.$$

ζ = -0.055 for rock salt $Mg_{0.2}Co_{0.2}Ni_{0.2}Cu_{0.2}Zn_{0.2}O$, while ζ = -1.117 for the Co_3O_4 spinel. An additional major anisotropic contribution comes from the estimated low-index interfacial energies ({100}: 0.92 J/m^2, {110}: 1.31 J/m^2, {111}: 2.31 J/m^2). When a crystal phase evolves in a constrained matrix, as in the present topotactic transformation, a more negative ζ parameter and strong anisotropic interfacial energies both favor the habit planes with {100} low index facets, explaining the cuboidal precipitate morphology in Figure 2K and Figure 6B.

4 | DISCUSSION AND OUTLOOK

Intentionally designed nanocomposite films represent a vast and dynamic field, encompassing a wide range of functionalities. These include metamaterials with plasmonic and hyperbolic optical properties, as well as ferromagnetic, ferroelectric, and multiferroic behaviors. Typically, nanocomposite films are formed through simultaneous deposition of multiple materials, layer-by-layer growth, or self-assembly. Self-assembled nanocomposites form spontaneously through strain and surface energy minimization between two different materials, organizing nanoparticles into well-defined structures without extensive external manipulation.[49–51] Therefore, while phase separation from a metastable solid solution to a multiphase ensemble has some established precedence, exploring these processes within an initially entropy-stabilized homogeneous single-phase host offers a novel and untapped pathway into materials engineering. The slow-to-fast and thin-to-thick deposition conditions explored in this PLD study provide kinetic access to an interesting set of topotactic nanostructures that evolve during experimental timescales. They occur through a chemical ordering process where either Cu or Co chemically segregate into lattice sites that offer a lower overall free energy at the expense of entropic disorder.

$Mg_{0.2}Co_{0.2}Ni_{0.2}Cu_{0.2}Zn_{0.2}O$ illustrates a diversity of chemical, structural, and defect chemistry nanostructures that involve both continuous (i.e., ordering while preserving coherent boundaries) and discontinuous formation paths. Prior work shows how thin film synthesis temperature alone can produce up to a 5% lattice constant swing without a structure transition while the present work details two distinct nanostructure ordering motifs. The interesting difference separating the possibilities is the degree and type of energy available to initiate order and the thermodynamic boundary conditions (i.e., oxygen activity and strain) that can bias the transition along a preferred path. It is difficult to find crystalline systems with simpler chemistry that exhibit such behavior. While non-existence cannot prove a hypothesis, in this case, it supports the possibility that high-entropy crystals, by virtue of their enormous configuration space, can access myriad microstates with a continuum of closely spaced free energies (as they serially adopt small degrees of order) that create pathways to the nanostructured crystals presently observed. It is additionally interesting to note the macroscopic tolerance for local disorder in these crystals. XRD (Figure 2A) shows examples where $Mg_{0.2}Co_{0.2}Ni_{0.2}Cu_{0.2}Zn_{0.2}O$ film is fully populated by spinel pockets with ~1% misfit strain, but X-ray line widths remain as narrow as the homogeneous parent solid solution, and the film remains pseudomorphic with almost no misfit interfacial dislocations. It appears possible that the diversity of locally ordered and disordered structures provides different mechanisms to minimize energy, which may be the unique, scientifically interesting, and technology-enabling cornerstone of the entropy-stabilized formulation. While we primarily focus on $Mg_{0.2}Co_{0.2}Ni_{0.2}Cu_{0.2}Zn_{0.2}O$ with CuO and Co_3O_4 exsolution, in theory, any cation confined within an entropy-stabilized structure that is thermodynamically unfavorable at temperatures below the entropic stabilization temperature could promote segregation and the formation of nano-morphologies.[31,52] Furthermore, it is also interesting and comforting that existing principles of crystal chemistry and thermodynamics can predictively explain this entire observation set. Phase-field models

capture the exsolved nanostructures with high chemical and structural fidelity.

While the entropy-stabilized random and homogeneous solid solution is the highest-entropy member of the structural continuum and it receives most experimental attention, it represents only one macrostate. In this manuscript, we show that in $Mg_{0.2}Co_{0.2}Ni_{0.2}Cu_{0.2}Zn_{0.2}O$, and likely many other high-entropy formulations, it is possible to deliberately and predictively "spend" entropy by synthesis, thermal history, and boundary condition combinations to metastabilize different macrostates along the ordering spectrum. We propose that each one represents a new material with a likelihood of new property opportunities and that the key to active material engineering in high-configuration space is understanding how formulation, structure, and process combine to regulate entropic spending.

5 | METHODS

5.1 | Sample synthesis

$Mg_{0.2}Co_{0.2}Ni_{0.2}Cu_{0.2}Zn_{0.2}O$ epitaxial films were grown using similar methods to those reported previously.[38] A single-phase ceramic ablation target was reactively sintered from a stoichiometric binary oxide powder mixture of MgO (≥99%), CoO (≥99%), NiO (99.99%), CuO (99.99%), and ZnO (99.999%) in air at 1000°C for 12 h and air-quenched to obtain a single rock salt phase. Thin films were deposited on [001]-MgO substrates by PLD using a Coherent 248 nm KrF laser. Substrates were cleaned with acetone, isopropanol, and methanol followed by a 10-min ultraviolet-ozone treatment then adhered to a block heater with silver paint (Ted Pella Leitsilber 200). The substrate temperature was 400°C to ensure relatively low T_{sub} ~400°C to preserve metastability and to avoid low-temperature enhanced Co^{3+} concentrations.[37] 25 sccm oxygen O_2 was flowed into the chamber, the gate valve was throttled until the chamber pressure stabilized at 50 mTorr. Laser fluence was 1.2 J/cm^2 with a total laser pulse energy of 170 mJ. All films were quenched to ambient lab conditions by venting the chamber to ambient air less than 2 min after the final laser pulse to mitigate post-synthesis annealing effects.

5.2 | Sample characterization

XRD was performed using a PANalytical Empyrean diffractometer. The primary incident beam optic was a hybrid mirror/2-bounce Ge monochromator combination, the primary diffracted beam optic was a programmable divergent slit and a PIXcel^{3D} detector combination. TEM samples were fabricated using a focused ion beam (FIB) approach. First, a 500 nm carbon layer was deposited with the electron beam to protect the top surface. A second 4 μm layer was subsequently deposited with the ion beam. Thin TEM lamella was milled using a 30 kV Ga ion beam lifted out in situ and mounted on a carbon FIB grid to avoid contamination. The samples were thinned with 30 and 5 kV Ga ion beams for electron transparency. The resulting lamellae were then cleaned with 2 kV and 1 kV Ga ion beams to reduce damage and amorphization.

SAED patterns and DF-TEM images were collected using a ThermoFisher Talos 200X TEM at 200 kV. ADF-STEM images, LAADF-STEM images, energy dispersive X-ray (EDX) spectra, and EELS were collected using a ThermoFisher Titan G2 aberration-corrected STEM at 300 kV. The convergence angle was 21.5 mrad, and the collection angle was 61–200 mrad for ADF-STEM mode and 26–149 mrad for LAADF-STEM mode. EELS spectra were collected in the dual-EELS mode with an energy resolution of around 0.18 eV, measured with the full-width half maxima of the zero-loss peak (ZLP). The EELS collection angle was 12.2 mrad.

TEM image analysis employed a physics-based deep data image analysis algorithm that can categorize local symmetry from atomically resolved imaging data to extract a priori unknown local distortions.[53,54] Subsequent data classification employed dimensionality reduction via principal component analysis (PCA), followed by data clustering using a Gaussian mixture model (GMM). A flowchart illustrating our procedure is shown in Figure S1. A cropping window with a height (h) and width (w) of 500 pixels was placed on an ADF-STEM image. The center position of the window was shifted across the entire image with the step size of 12 pixels, and sub-images were cropped at each position forming a stack of sub-images with three dimensions (h by w by n). The positions of the cropping window were recorded as (xp, yp). Next, a 2D FT was performed on each sub-image, and this step generated a stack of FT patterns that represent the local periodicity of the crystal. The stack of FT patterns was then flattened into two dimensions (h • w by n). For PCA, the stack of FT patterns was categorized into four, three, or two classes for STEM images collected from 6000–1, 1200–1, or 6000–5 Hz films, respectively. Class-averaged FT patterns were extracted by averaging the FT patterns within each class. Finally, image segregation was performed by projecting the corresponding cropping window positions back to the original STEM image and overlaid with color based on the class.

The STEM-EELS analysis was performed using an unsupervised machine learning algorithm. Each EELS spectrum was corrected based on the ZLP position.

The unsupervised machine learning algorithm included dimensionality reduction with nonnegative matrix factorization (NMF) and clustering with GMM using the *fitgmdist* MATLAB function.[55] During the STEM-EELS experiment, three-dimensional spectral image data (h by w by 2048 channels) was acquired from the area of interest. The spectral image was flattened into two dimensions (h•w by 2048), and the dimensionality reduction was performed to decompose the data into a linear combination defined by two loading vectors (2 by 2048) and the corresponding scores (h•w by 2). The clustering with GMM was performed on the NMF scores, and the spectral image data was clustered into two classes. The class-averaged spectra were then extracted based on the clustering results.

5.3 | Computational methods

The phase-field method is a mesoscale density-based computational method that allows modeling microstructural temporal evolution during materials processes (Note S6).[56] Phase-field simulations were carried out with the semi-implicit Fourier-spectral method[57] which has been applied to solve the time-dependent Allen-Cahn and diffusion equations with periodic boundary conditions as described in the supplemental materials.[22,56] We note that our models capture the growth and coarsening stages of two nanostructure types within the rock salt matrix. Each simulation minimizes the total free energy as a function of order parameters representing the phase distributions and cation concentrations. The order parameters' initial distribution is given by random fields, while the initial chemical concentrations are homogeneous for each simulation. 3D simulations of $(120\ \text{nm})^3$ were used to model the CuO-rich nanotweed and spinel nano-cuboids, which are discretized into $1\ \text{nm}^3$ cubic grids. A 2D slice was utilized for the nanotweed for ease of interpretation. The total free energy considers the chemical potentials, elastic strain energies, and interfacial energies. Elastic stiffness and stress-free strain values were calculated using DFT (Note S7). For the CuO-rich tweed simulations, we employed experimental strain values due to the overestimation of stress-free DFT calculations. The magnitude of rock salt-spinel interfacial energies are approximated using the reported value for {100} CoO / {100} Co_3O_4 from Chen et al.,[58] while the anisotropy is incorporated using relative ratios of Co_3O_4 low-index surface energies.[59]

ACKNOWLEDGMENTS

The authors gratefully acknowledge support from NSF MRSEC DMR-2011839. The authors would also like to acknowledge many helpful and enlightening discussions with Susan Trolier-McKinstry, John T. Heron, Venkatraman Gopalan, and Zhiqiang Mao regarding the nuances of high-entropy systems. Phase-field simulations and DFT calculations utilized resources from the ROAR cluster of the Penn State Institute for Computational and Data Sciences.

ORCID

Saeed S. I. Almishal https://orcid.org/0000-0003-2964-6000
Leixin Miao https://orcid.org/0000-0002-5454-5765
George N. Kotsonis https://orcid.org/0000-0003-2939-0746
Long-Qing Chen https://orcid.org/0000-0003-3359-3781
Jon-Paul Maria https://orcid.org/0000-0003-3604-4761

REFERENCES

1. Ranganathan S. Alloyed pleasures: multimetallic cocktails. Curr. Sci. 2003;85:1404–6.
2. Murty BS, Yeh J-W, Ranganathan S, Bhattacharjee PP. High-entropy alloys. Amsterdam, NL: Elsevier; 2019.
3. Kotsonis GN, Almishal SSI, Marques dos Santos Vieira F, Crespi VH, Dabo I, Rost CM, et al. High-entropy oxides: harnessing crystalline disorder for emergent functionality. J Am Ceram Soc. 2023;106:5587–611. https://doi.org/10.1111/jace.19252
4. Hernandez FCR, Ramírez JMH, Mackay R. Al-Si alloys: automotive, aeronautical, and aerospace applications. Switzerland: Springer; 2017.
5. Singh R, Oprysko MM, Harame DL. Silicon germanium: technology, modeling, and design. Hoboken, NJ: John Wiley & Sons; 2004.
6. Farrell RM, Hsu PS, Haeger DA, Fujito K, DenBaars SP, Speck JS, et al. Low-threshold-current-density AlGaN-cladding-free m-plane InGaN/GaN laser diodes. Appl Phys Lett. 2010;96:231113. https://doi.org/10.1063/1.3443719
7. Li F, Cabral MJ, Xu B, Cheng Z, Dickey EC, LeBeau JM, et al. Giant piezoelectricity of Sm-doped $Pb(Mg_{1/3}Nb_{2/3})O_3$-$PbTiO_3$ single crystals. Science. 2019;364:264–68. https://doi.org/10.1126/science.aaw2781
8. Fichtner S, Wolff N, Lofink F, Kienle L, Wagner B. AlScN: a III-V semiconductor based ferroelectric. J Appl Phys. 2019;125:114103. https://doi.org/10.1063/1.5084945
9. Hayden J, Hossain MD, Xiong Y, Ferri K, Zhu W, Imperatore MV, et al. Ferroelectricity in boron-substituted aluminum nitride thin films. Phys Rev Mater. 2021;5:044412. https://doi.org/10.1103/PhysRevMaterials.5.044412
10. Adachi S. GaAs, AlAs, and $Al_xGa_{1-x}As$: material parameters for use in research and device applications. J Appl Phys. 1985;58:R1–R29. https://doi.org/10.1063/1.336070
11. Berlincourt D, Cmolik C, Jaffe H. Piezoelectric properties of polycrystalline lead titanate zirconate compositions. Proc IRE. 1960;48:220–29. https://doi.org/10.1109/JRPROC.1960.287467
12. Goldschmidt V. The laws of crystal chemistry. Nat Sci. 1926;14:477–85.
13. Hume-Rothery W, Powell HM. On the theory of super-lattice structures in alloys. J Crystallogr – Crystall Mater. 1935;91:23–47.

14. Pauling L. The sizes of ions and the structure of ionic crystals. J Am Chem Soc. 1927;49:765–90.
15. Megaw HD. Crystal structures: a working approach. Philadelphia, PA: W.B. Saunders; 1973.
16. Muller O, Roy R. The major ternary structural families. Berlin: Springer-Verlag; 1974.
17. Cantor B, Chang ITH, Knight P, Vincent AJB. Microstructural development in equiatomic multicomponent alloys. Mater Sci Eng A. 2004;375–377:213–18. https://doi.org/10.1016/j.msea.2003.10.257
18. Yeh J, Chen S, Lin S, Gan J, Chin T, Shun T, et al. Nanostructured high-entropy alloys with multiple principal elements: novel alloy design concepts and outcomes. Adv Eng Mater. 2004;6:299–303.
19. Rost CM, Sachet E, Borman T, Moballegh A, Dickey EC, Hou D, et al. Entropy-stabilized oxides. Nat Commun. 2015;6:8485. https://doi.org/10.1038/ncomms9485
20. Sarkar A, Wang Q, Schiele A, Chellali MR, Bhattacharya SS, Wang D, et al. High-entropy oxides: fundamental aspects and electrochemical properties. Adv Mater. 2019;31:e1806236. https://doi.org/10.1002/adma.201806236
21. Aamlid SS, Oudah M, Rottler J, Hallas AM. Understanding the role of entropy in high entropy oxides. J Am Chem Soc. 2023;145:5991–6006. https://doi.org/10.1021/jacs.2c11608
22. Khachaturyan A. Theory of structural transformations in solids. Mineola, NY: Courier Corporation; 2008.
23. Rost CM, Rak Z, Brenner DW, Maria J-P. Local structure of the $Mg_xNi_xCo_xCu_xZn_xO(x = 0.2)$ entropy-stabilized oxide: an EXAFS study. J Am Ceram Soc. 2017;100:2732–38. https://doi.org/10.1111/jace.14756
24. Diercks DR, Brennecka G, Gorman BP, Rost CM, Maria J-P. Nanoscale compositional analysis of a thermally processed entropy-stabilized oxide via correlative TEM and APT. Microsc Microanal. 2017;23:1640–41. https://doi.org/10.1017/S1431927617008868
25. Bhaskar LK, Nallathambi V, Kumar R. Critical role of cationic local stresses on the stabilization of entropy-stabilized transition metal oxides. J Am Ceram Soc. 2020;103:3416–24. https://doi.org/10.1111/jace.17029
26. Dupuy AD, Wang X, Schoenung JM. Entropic phase transformation in nanocrystalline high entropy oxides. Mater Res Lett. 2019;7:60–67. https://doi.org/10.1080/21663831.2018.1554605
27. Zhang J, Yan J, Calder S, Zheng Q, McGuire MA, Abernathy DL, et al. Long-range antiferromagnetic order in a rocksalt high entropy oxide. Chem Mater. 2019;31:3705–11. https://doi.org/10.1021/acs.chemmater.9b00624
28. Pitike KC, KC S, Eisenbach M, Bridges CA, Cooper VR. Predicting the phase stability of multicomponent high-entropy compounds. Chem Mater. 2020;32:7507–15. https://doi.org/10.1021/acs.chemmater.0c02702
29. Anand G, Wynn AP, Handley CM, Freeman CL. Phase stability and distortion in high-entropy oxides. Acta Mater. 2018;146:119–25. https://doi.org/10.1016/j.actamat.2017.12.037
30. Sivak JT, Almishal SSI, Caucci MK, Tan Y, Srikanth D, Furst M, et al. Discovering high-entropy oxides with a machine-learning interatomic potential. arXiv. 2024. https://doi.org/10.48550/arXiv.2408.06322
31. Almishal SSI, Sivak JT, Kotsonis GN, Tan Y, Furst M, Srikanth D, et al. Untangling individual cation roles in rock salt high-entropy oxides. Acta Mater. 2024;279:120289. https://doi.org/10.1016/j.actamat.2024.120289
32. Musicó B, Wright Q, Ward TZ, Grutter A, Arenholz E, Gilbert D, et al. Tunable magnetic ordering through cation selection in entropic spinel oxides. Phys Rev Mater. 2019;3:104416. https://doi.org/10.1103/PhysRevMaterials.3.104416
33. Witte R, Sarkar A, Kruk R, Eggert B, Brand RA, Wende H, et al. High-entropy oxides: an emerging prospect for magnetic rare-earth transition metal perovskites. Phys Rev Mater. 2019;3:034406. https://doi.org/10.1103/PhysRevMaterials.3.034406
34. Mazza AR, Skoropata E, Sharma Y, Lapano J, Heitmann TW, Musico BL, et al. Designing magnetism in high entropy oxides. Adv Sci. 2022;9:2200391.
35. Johnstone GHJ, González-Rivas MU, Taddei KM, Sutarto R, Sawatzky GA, Green RJ, et al. Entropy engineering and tunable magnetic order in the spinel high-entropy oxide. J Am Chem Soc. 2022;144:20590–600. https://doi.org/10.1021/jacs.2c06768
36. Sarkar A, Eggert B, Witte R, Lill J, Velasco L, Wang Q, et al. Comprehensive investigation of crystallographic, spin-electronic and magnetic structure of $(Co_{0.2}Cr_{0.2}Fe_{0.2}Mn_{0.2}Ni_{0.2)3}O_4$: unraveling the suppression of configuration entropy in high entropy oxides. Acta Mater. 2022;226:117581. https://doi.org/10.1016/j.actamat.2021.117581
37. Kotsonis GN, Meisenheimer PB, Miao L, Roth J, Wang B, Shafer P, et al. Property and cation valence engineering in entropy-stabilized oxide thin films. Phys Rev Mater. 2020;4:100401. https://doi.org/10.1103/PhysRevMaterials.4.100401
38. Meisenheimer PB, Williams LD, Sung SH, Gim J, Shafer P, Kotsonis GN, et al. Magnetic frustration control through tunable stereochemically driven disorder in entropy-stabilized oxides. Phys Rev Mater. 2019;3:104420. https://doi.org/10.1103/PhysRevMaterials.3.104420
39. Lun Z, Ouyang B, Kwon D-H, Ha Y, Foley EE, Huang T-Y, et al. Cation-disordered rocksalt-type high-entropy cathodes for Li-ion batteries. Nat Mater. 2021;20:214–21. https://doi.org/10.1038/s41563-020-00816-0
40. Zhai S, Rojas J, Ahlborg N, Lim K, Toney MF, Jin H, et al. The use of poly-cation oxides to lower the temperature of two-step thermochemical water splitting. Energy Environ Sci. 2018;11:2172–78.
41. Kotsonis GN, Almishal SSI, Miao L, Caucci MK, Bejger GR, Ayyagari SVG, et al. Fluorite-structured high-entropy oxide sputtered thin films from bixbyite target. Appl Phys Lett. 2024;124:171901. https://doi.org/10.1063/5.0201419
42. Spurling RJ, Almishal SSI, Casamento J, Hayden J, Spangler R, Marakovits M, et al. Dielectric properties of disordered $A_6B_2O_{17}$ (A = Zr; B = Nb, Ta) phases. J Am Ceram Soc. 2024;107:6868–75. https://doi.org/10.48550/arXiv.2405.03527
43. DAVIES PK. Investigations of NiO-CuO Solid Solutions using transmission electron microscopy: I, tweed microstructure. J Am Ceram Soc. 1986;69:796–99. https://doi.org/10.1111/j.1151-2916.1986.tb07362.x
44. Zhu Y, Cai Z-X. Diffuse scattering and image contrast of tweed in superconducting oxides: simulation and interpretation. Ultramicroscopy. 1993;52:539–48. https://doi.org/10.1016/0304-3991(93)90071-5
45. Berardan D, Meena AK, Franger S, Herrero C, Dragoe N. Controlled Jahn-Teller distortion in (MgCoNiCuZn)O-based high

entropy oxides. J Alloys Compd. 2017;704:693–700. https://doi.org/10.1016/j.jallcom.2017.02.070
46. Rák Zs, Maria J-P, Brenner DW. Evidence for Jahn-Teller compression in the (Mg, Co, Ni, Cu, Zn)O entropy-stabilized oxide: a DFT study. Mater Lett. 2018;217:300–303. https://doi.org/10.1016/j.matlet.2018.01.111
47. Hazen RM, Jeanloz R. Wüstite ($Fe_{1-x}O$): A review of its defect structure and physical properties. Rev Geophys. 1984;22:37–46. https://doi.org/10.1029/RG022i001p00037
48. Gao P, Ishikawa R, Tochigi E, Kumamoto A, Shibata N, Ikuhara Y. Atomic-scale tracking of a phase transition from spinel to rocksalt in lithium manganese oxide. Chem Mater. 2017;29:1006–13. https://doi.org/10.1021/acs.chemmater.6b03659
49. Misra S, Wang H. Review on the growth, properties and applications of self-assembled oxide–metal vertically aligned nanocomposite thin films—current and future perspectives. Mater Horiz. 2021;8(3):869-84.
50. Nan C-W, Jia Q. Obtaining ultimate functionalities in nanocomposites: design, control, and fabrication. MRS Bull. 2015;40:719–24. https://doi.org/10.1557/mrs.2015.196
51. Łapiński M, Kozioł R, Skubida W, Winiarz P, Mahjoub Yahia Elhassan R, Sadowski W, et al. Transformation of bimetallic Ag–Cu thin films into plasmonically active composite nanostructures. Sci Rep. 2023;13:10107. https://doi.org/10.1038/s41598-023-37343-2
52. Niculescu GE, Bejger GR, Barber JP, Wright JT, Almishal SSI, Webb M, et al. Local structure maturation in high entropy oxide $(Mg,Co,Ni,Cu,Zn)_{1-x}(Cr,Mn)_xO$ thin films. J Am Ceram Soc. 2024:e20171. https://doi.org/10.1111/jace.20171
53. Vasudevan RK, Ziatdinov M, Jesse S, Kalinin SV. Phases and interfaces from real space atomically resolved data: physics-based deep data image analysis. Nano Lett. 2016;16:5574–81. https://doi.org/10.1021/acs.nanolett.6b02130
54. Somnath S, Smith CR, Kalinin SV, Chi M, Borisevich A, Cross N, et al. Feature extraction via similarity search: application to atom finding and denoising in electron and scanning probe microscopy imaging. Adv Struct Chem Imag. 2018;4:3. https://doi.org/10.1186/s40679-018-0052-y
55. McLachlan GJ, Lee SX, Rathnayake SI. Finite mixture models. Ann Rev Stat Appl. 2019;6:355-78.
56. Chen LQ, Zhao Y. From classical thermodynamics to phase-field method, Prog Mater Sci. 2022;124:100868.
57. Chen LQ, Shen J. Applications of semi-implicit Fourier-spectral method to phase field equations. Comput Phys Commun. 1998;108:147–58. https://doi.org/10.1016/S0010-4655(97)00115-X
58. Chen X, Van Gog H, Van Huis MA. Transformation of Co_3O_4 nanoparticles to CoO monitored by in situ TEM and predicted ferromagnetism at the Co_3O_4/CoO interface from first principles, J Mater Chem C. 2021;9:5662–75.
59. Ribeiro RAP, De Lazaro SR, Gracia L, Longo E, Andrés J. Theoretical approach for determining the relation between the morphology and surface magnetism of Co_3O_4. J Magn Magn Mater. 2018;453:262–67. https://doi.org/10.1016/j.jmmm.2017.11.025

SUPPORTING INFORMATION

Additional supporting information can be found online in the Supporting Information section at the end of this article.

How to cite this article: Almishal SSI, Miao L, Tan Y, Kotsonis GN, Sivak JT, Alem N, et al. Order evolution from a high-entropy matrix: Understanding and predicting paths to low-temperature equilibrium. J Am Ceram Soc. 2025;108:e20223. https://doi.org/10.1111/jace.20223